Optics Letters

Radially and azimuthally polarized nanosecond Yb-doped fiber MOPA system incorporating temporal shaping

D. Lin,* N. Baktash, M. Berendt, M. Beresna, P. G. Kazansky, W. A. Clarkson, S. U. Alam, and D. J. Richardson

Optoelectronics Research Centre, University of Southampton, Southampton SO17 1BJ, UK
**Corresponding author: Di.Lin@soton.ac.uk*

Received 12 January 2017; revised 27 February 2017; accepted 7 March 2017; posted 13 March 2017 (Doc. ID 284648); published 24 April 2017

We report an Yb-doped fiber master-oscillator power-amplifier (MOPA) system with the capability of selectively generating doughnut-shaped radially and azimuthally polarized beams with user-defined temporal pulse shapes. The desired output polarization was generated with the aid of a nanograting spatially variant half-waveplate (S-waveplate). The latter was used to convert the linearly polarized fundamental (LP_{01}) mode output from the preamplification stages to a doughnut-shaped radially polarized beam prior to the power amplifier stage. A maximum output pulse energy of ~860 μJ was achieved for ~100 ns pulses at 25 kHz with user-defined pulse shape for both radial and azimuthal polarization states. The polarization purity and beam propagation factor (M^2) were measured to be >12 dB and 2.2, respectively.

OCIS codes: (140.3510) Lasers, fiber; (060.2320) Fiber optics amplifiers and oscillators; (140.3300) Laser beam shaping; (320.5540) Pulse shaping.

https://doi.org/10.1364/OL.42.001740

Cylindrical vector beams characterized by cylindrically symmetric spatial polarization distributions across the beam cross-section have attracted considerable attention in recent years because of their unique optical properties. Radially and azimuthally polarized beams, a subclass of cylindrical vector beams, are of great interest for a wide range of applications, including high-resolution microscopy [1], particle manipulation [2], and material processing [3]. Various methods have been developed to generate cylindrical vector beams for continuous-wave and pulsed operation of solid-state bulk lasers [4], thin-disk lasers and amplifiers [5,6], and fiber lasers and amplifiers [7–9]. In the nanosecond regime, these unique beams have been generated directly from both *Q*-switched solid-state and fiber lasers, and their advantages for various laser processing applications have been the subject of much study [10]. Diode-seeded fiber-based master-oscillator power-amplifier (MOPA) systems have been shown to provide versatile nanosecond pulse sources offering mJ-level pulse energies with high average and peak powers. The great flexibility they offer in terms of modifying both pulse duration and pulse repetition rate has facilitated widespread use of such systems in applications such as material processing. Moreover, the ability to generate user-defined temporal pulse shapes can improve the energy efficiency and the quality of laser machining [11]. Since the vector TM_{01} and TE_{01} modes in circular core fibers have radial and azimuthal polarization states, respectively, it is possible to generate these unique beams from a fiber MOPA system while maintaining the capability of controlling the temporal pulse shape to benefit materials processing.

In this Letter, for the first time to the best of our knowledge, we present an Yb-doped fiber (YDF) MOPA system for efficiently generating high-energy radially and azimuthally polarized nanosecond pulses. The system is seeded by a directly modulated super-luminescent diode (SLD) to generate nanosecond pulses with user-defined temporal pulse shapes at 25 kHz repetition rate. The spatial mode shaping is achieved by using an S-waveplate to convert the linearly polarized fundamental (LP_{01}) mode from the preamplification stages into a doughnut-shaped radially polarized beam prior to the power amplifier.

A schematic of the experimental set-up is shown in Fig. 1. It consists of a four-stage YDF amplifier chain, the first three amplifiers of which are fully fiberized. An SLD operating at a central wavelength of ~1030 nm with 3 dB bandwidth of 20 nm is used as the seed laser and can deliver up to 150 mW of peak power. The SLD was mounted on a commercial drive board (PicoLas, BFS-VRM 03 HP) and was directly modulated using a computer-controlled arbitrary waveform generator (AWG), which has a 12 GHz sampling rate and 10-bit amplitude resolution. The pulse duration can be adjusted from 1 ns at a maximum repetition rate of 500 MHz to continuous-wave as desired. For the experiments described in this Letter, the seed

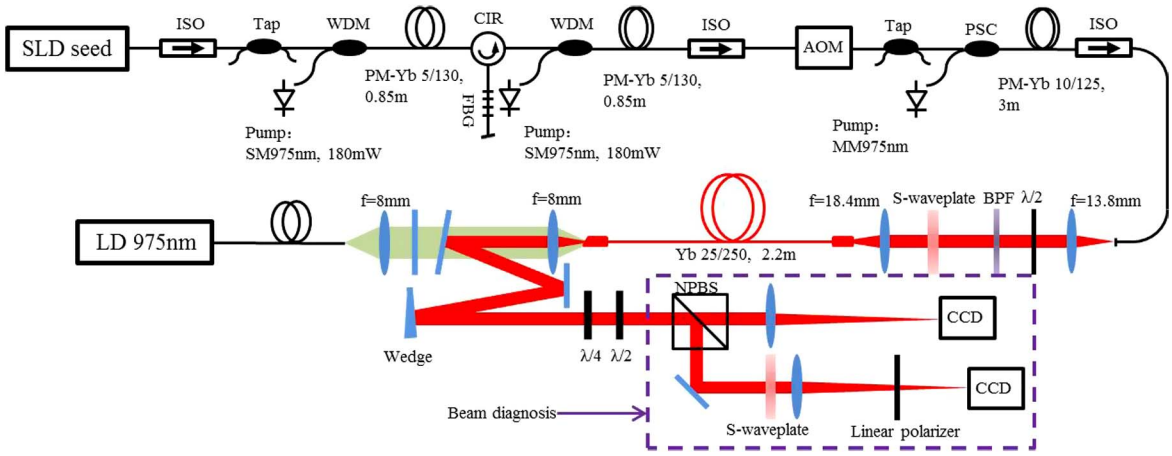

Fig. 1. Schematic of the experimental setup for amplifying cylindrical vector beams using an Yb-doped fiber MOPA system and the output beam diagnostics. ISO, optical isolator; WDM, wavelength division multiplexer; AOM, acoustic optical modulator; PSC, pump and signal combiner; CIR, circulator; CCD, charged coupled device; BPF, bandpass filter; NPBS, non-polarization beam splitter.

pulse duration and repetition rate were set at 100 ns and 25 kHz, respectively. The significance of the use of the SLD is that it substantially increases the robustness of the system by raising the threshold for stimulated Brillouin scattering (SBS) induced damage. The first preamplifier stage consists of an 85-cm-long length of polarization maintaining Yb-doped fiber (PM-YDF) that has a 5 μm core diameter with a numerical aperture (NA) of 0.12 and 130 μm cladding diameter with an NA of 0.46. It was forward core-pumped by a 975 nm single-mode laser diode to amplify the pulses to ∼14 mW average power (gain ∼22 dB). A uniform pitch fiber Bragg grating (FBG) with a high reflectivity of >99% at the center wavelength of 1040.5 nm and with a 3 dB bandwidth of 0.25 nm was spliced after the first preamplifier stage to spectrally slice the amplified pulse spectrum, resulting in a total loss of ∼20 dB. The second preamplifier, having a similar configu ration to the first preamplifier, amplified the average power of the spectrally sliced pulses to ∼18 mW. A fiber-pigtailed acousto-optic modulator (AOM) was used for pulse picking and to remove the amplified spontaneous emission (ASE) between pulses. This resulted in an average power of ∼12 mW with which to seed the third preamplifier stage. The third preamplifier consists of a 3-m-long PM-YDF with a core diameter of 10 μm and an NA of 0.075 and a cladding diameter of 125 μm and a corresponding NA of 0.46. This amplifier was forward cladding pumped with a 975 nm multimode laser diode. A free-space bandpass filter (BPF) with a 3 dB bandwidth of 4 nm was inserted after the third preamplifier to remove any excess ASE, resulting in a linearly polarized Gaussian-shaped LP_{01} output beam with a pulse energy of ∼11 μJ and a polarization extinction ratio (PER) of >20 dB.

The final amplifier comprises a 2.2-m-long commercial few-mode YDF (Liekki Yb1200-25/250), which has a core diameter of 25 μm and an NA of 0.07 and an inner cladding of diameter 250 μm with an NA of 0.46. The V-number of the YDF at 1040.5 nm is ∼5.28, which is large enough to support the propagation of both TM_{01} and azimuthally polarized TE_{01} modes. The pump beam was provided by a fiber-coupled 975 nm laser diode, which was free-space coupled into the YDF fiber in a counter-pumped configuration. The pump absorption was measured to be ∼92%. To prevent optical damage at the air–silica interface and to suppress parasitic oscillations, both ends of the fiber were spliced to endcaps with a diameter of 250 μm and a length of ∼1.5 mm. The input end facet was perpendicularly cleaved to ensure that the radially polarized doughnut-shaped beam was coupled into the fiber core without any spatial distortion, and the output end facet was angle-cleaved with an angle of ∼8 deg. A half-wave plate and an S-waveplate were placed before the final amplifier to convert the incident linearly polarized Gaussian-shaped beam into a radially polarized doughnut-shaped beam that was then coupled into the few-moded YDF to excite the TM_{01} mode. A detailed description of the working principles for the S-waveplate can be found in [12]. Because of the ∼1.2 dB insertion loss of the S-waveplate and ∼2 dB coupling loss, ∼5 μJ of radially polarized beam was successfully coupled into the final stage amplifier. Given that the effective index differences of the four vector modes (TM_{01}, TE_{01}, HE_{21e}, and HE_{21o} modes) in the LP_{11} mode group are relatively small ($<10^{-5}$) in weakly guiding standard circular core fibers, severe mode coupling is expected even for the case of small external perturbation. To reduce the intermodal coupling, the fiber was loosely coiled with a large bend diameter of ∼25 cm, and any twist to the fiber was avoided.

After optimizing the beam launching conditions and carefully manipulating the few-mode YDF to reduce the intermodal coupling, a doughnut-shaped output beam was successfully achieved, which was monitored using a CCD camera. Fig. 2(a) shows the average output power and pulse energy of the doughnut-shaped output beam as a function of the launched pump power to the final amplifier. The average output power reached a maximum of 22.5 W with a slope efficiency of ∼66% with respect to the launched pump power. The maximum pulse energy was simultaneously measured to be ∼860 μJ with the aid of an energy meter (Ophir PE9-C), indicating that the ASE fraction was less than 5% of the total output power. The gain of the final amplifier reached ∼22 dB, and an overall gain of ∼55 dB was obtained along the whole MOPA system. Further increase in pump power resulted in the parasitic lasing of the fundamental LP_{01} mode, and this limited the maximum extractable pulse energy. This

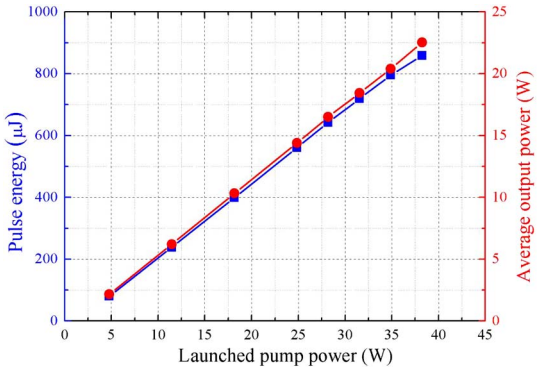

Fig. 2. Pulse energy and average output power as a function of the launched pump power to the final amplifier.

parasitic lasing is attributed to residual feedback from the end-caps in conjunction with the high gain associated with undepleted population inversion at the center of the fiber core due to the null in intensity for the doughnut-shaped beam.

Temporal pulse shaping was simultaneously achieved using the adaptive pulse shaping technique. The preshaped seed pulse was generated by directly modulating the drive current of the SLD through the computer-controlled AWG according to the Frantz–Nodvik equation to compensate for the pulse distortion due to gain saturation within the MOPA system. A detailed description of this technique can be found in [13]. As an exemplar pulse shape we generated two-step pulse shapes that have previously been shown to be advantageous in machining materials such as silicon. Fig. 3 shows two examples of two-step pulses with the same duration of 100 ns. Both pulse shapes had a similar pulse energy of ~860 μJ, but the energy was distributed differently between the two steps within each pulse. In the first example, a 39 kW pulse peak power was maintained for 6.4 ns (full width at half-maximum [FWHM]), followed by 7 kW for 87 ns, while in the second example, 26 kW was maintained for 14 ns, followed by 6 kW for 80 ns. The spectra of two-step pulses with the 14 ns leading spike at different amplifier stages are shown in Fig. 4, measured using an optical spectrum analyzer (OSA) (YOKOGAWA AQ6370D) at a resolution of 0.02 nm. The 3 dB spectral bandwidth was broadened from 0.02 nm (after the FBG) to 0.6 nm (output) due to self-phase modulation (SPM) induced by the high peak powers.

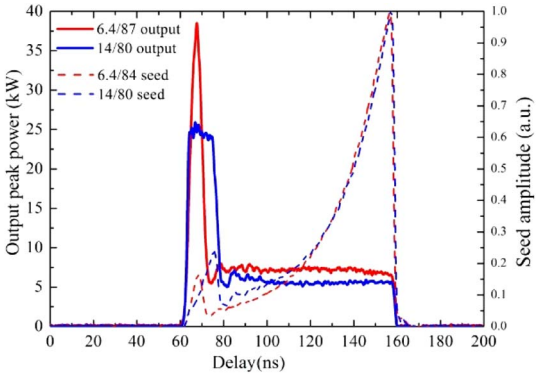

Fig. 3. Spectra of the 14 ns/80 ns two-step pulse measured after the FBG (black), 3rd stage preamplifier (blue) and at the output of the MOPA with a pulse energy of ~860 μJ. (*R*esolution = 0.02 nm.)

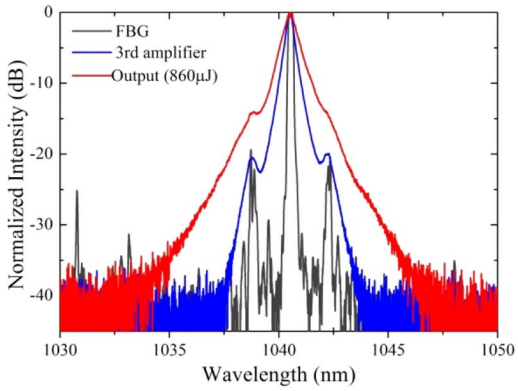

Fig. 4. Normalized pulse shapes after the SLD (dashed lines) and the corresponding output peak powers (solid lines) for two different two-step pulses.

Fig. 5(a) shows the far-field intensity distributions of the output beams at the maximum pulse energy of ~860 μJ. It is clear that the output beam exhibits a doughnut shape with an intensity null at the beam center. The slight ellipticity of the beam profile apparent in Fig. 5 is believed to be due to the slightly curved surface of the angle-cleaved output end facet. The polarization state of the doughnut-shaped output beam was first analyzed with the aid of a linear polarizer where the transmitted axis was rotated at different angles. In theory, the intensity distributions of a radially (or azimuthally) polarized beam after passing through a rotated linear polarizer exhibit symmetric two-lobe feature aligned parallel (or orthogonal) to the transmission axis of the polarizer. Figs. 5(b)–5(e) show the intensity distribution of the output beam after passing through a rotated linear polarizer, and the white arrow indicates the orientation of the transmission axis of the polarizer (0, 45, 90, and 135 deg). It is clear that the axis of the two-lobe-structured intensity distribution is not perfectly parallel to the axis of the linear polarizer, indicating that the radially polarized input beam has experienced change in polarization

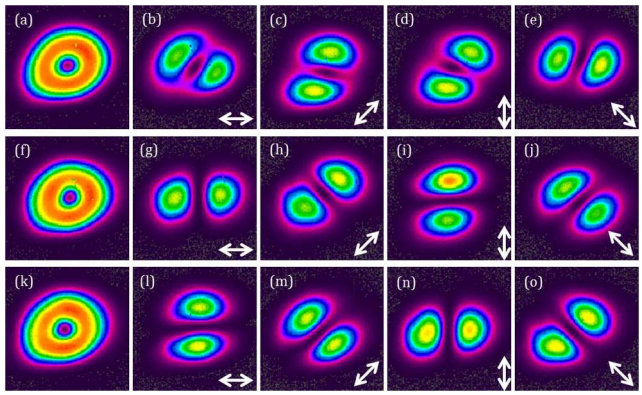

Fig. 5. Experimentally observed intensity distributions of the original output beam (top row), the radially polarized output beam (second row), and the azimuthally polarized output beam (bottom row) at the maximum pulse energy of ~860 μJ. (a), (f), and (k) show total intensity profiles. (b)–(e), (g)–(j), and (l)–(o) show beam profiles after passing through a rotated linear polarizer. The white arrows indicate the transmission axis of the polarizer.

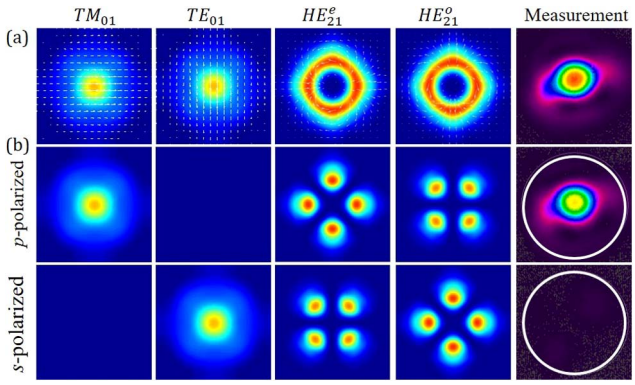

Fig. 6. Theoretical beam profiles for TM_{01}, TE_{01}, HE_{21e}, and HE_{21o} modes after the S-waveplate (a) without and (b) with the linear polarizer for orthogonal *s*- and *p*-polarization directions. The corresponding measured profiles on the right confirm high radial polarization purity.

during passage through the final stage amplifier due to strong mode coupling between the four nearly degenerate vector modes in the LP_{11} mode group. The mode coupling can be attributed to the residual birefringence of the fiber core due to imperfection in the fiber fabrication process, any residual stress applied to the fiber core when coiling the fiber, and thermally induced variation of the refractive index of the fiber core. It is worth mentioning that the doughnut-shaped intensity distribution was well maintained, while the polarization state changed slightly with variation of the output power. The polarization change could be successfully compensated (over extended operating periods) to regain high radial polarization purity using a combination of appropriately orientated quarter-wave and half-wave plates as shown in Fig. 5(f). The symmetric two-lobe-structured intensity distributions parallel to the transmission axis of the linear polarizer [shown in Figs. 5(g)–5(j)] confirm that the resultant output beam was radially polarized. Moreover, under these operating conditions, a simple adjustment of the orientation of the fast axis of the half-wave plate by a further 45 deg yielded an azimuthally polarized output beam [shown in Fig. 5(k)]. The azimuthal polarization state is verified through the symmetric two-lobe-structured intensity distributions orthogonal to the transmission axis of the linear polarizer as shown in Figs. 5(l)–5(o). The beam propagation factor (M^2) was measured to be approximately 2.2 at the maximum output power, in close agreement with the theoretical value of 2 for a doughnut-shaped radially polarized TM_{01} mode.

The radial/azimuthal polarization purity can be quantified by the mode extinction ratio (MER), which was investigated by making use of a vector mode decomposition technique [14]. An S-waveplate together with a linear polarizer were used to differentiate the four vector modes in the LP_{11} group. The S-waveplate, if properly aligned, converts the TM_{01} (TE_{01}) mode into a *p*-polarized (*s*-polarized) Gaussian-shaped beam in the far-field and converts the HE_{21o} and HE_{21e} modes to the higher order doughnut-shaped beams, which have the same intensity distribution but orthogonal polarization states in the far-field. The calculated intensity distributions of the four vector modes after passing through the S-waveplate and the corresponding intensity distributions in the *p*- and *s*-polarizations are shown in Fig. 6. The value of MER for the TM_{01} mode can be calculated by the ratio of power in the *p*-polarization to the *s*-polarization ($10\log(P_p/P_s)$). The fifth column of Fig. 6 shows experimental results for the radially polarized output beam at ~860 μJ, which were measured by the CCD camera. It is clear that the beam intensity in the *s*-polarization is much lower compared with the *p*-polarization. The power in each polarization direction was calculated by integrating the intensity within the white circle. The value of MER was measured to be >12 dB at all output power levels, confirming that a radially polarized output beam with high polarization purity was achieved. It is worth mentioning that the MER decreased from ~17.4 dB at ~100 μJ to ~12 dB at ~860 μJ. The presence of ASE slightly degraded the value of MER by ~2 dB at the maximum pulse energy.

In conclusion, we have demonstrated for the first time a directly modulated SLD seeded YDF MOPA system with spatial and temporal pulse-shaping capability. ~860 μJ nanosecond pulses at a repetition rate of 25 kHz with user-defined output pulse shapes as well as radially and azimuthally polarized doughnut-shaped beams have been achieved. Such a spatially and temporally flexible laser source is expected to be attractive and enabling for a variety of laser material processing and imaging applications.

The data from this Letter are available at repository http://doi.org/10.5258/SOTON/403975.

Funding. Engineering and Physical Sciences Research Council (EPSRC) (EP/M014029/1, EP/P012248/1).

REFERENCES

1. D. P. Biss and T. G. Brown, Opt. Lett. **28**, 923 (2003).
2. Q. Zhan, Opt. Express **12**, 3377 (2004).
3. R. Weber, A. Michalowski, M. Abdou-Ahmed, V. Onuseit, V. Rominger, M. Kraus, and T. Graf, Phys. Procedia **12**, 21 (2011).
4. I. Moshe, S. Jackel, A. Meir, Y. Lumer, and E. Leibush, Opt. Lett. **32**, 47 (2007).
5. M. A. Ahmed, M. Haefner, M. Vogel, C. Pruss, A. Voss, W. Osten, and T. Graf, Opt. Express **19**, 5093 (2011).
6. A. Loescher, J. P. Negel, T. Graf, and M. A. Ahmed, Opt. Lett. **40**, 5758 (2015).
7. D. Lin, K. G. Xia, R. X. Li, X. J. Li, G. Q. Li, K. Ueda, and J. L. Li, Opt. Lett. **35**, 3574 (2010).
8. D. Lin, J. M. O. Daniel, M. Gecevicius, M. Beresna, P. G. Kazansky, and W. A. Clarkson, Opt. Lett. **39**, 5359 (2014).
9. S. Kanazawa, Y. Kozawa, and S. Sato, Opt. Lett. **39**, 2857 (2014).
10. M. Meier, V. Romano, and T. Feurer, Appl. Phys. A **86**, 329 (2007).
11. K. Pangovski, M. Sparkes, A. Cockburn, W. O'Neill, P. S. Teh, L. D. Lin, and D. Richardson, IEEE J. Sel. Top. Quantum Electron. **20**, 51 (2014).
12. M. Beresna, M. Gecevicius, P. G. Kazansky, and T. Gertus, Appl. Phys. Lett. **98**, 201101 (2011).
13. A. Malinowski, K. T. Vu, K. K. Chen, J. Nilsson, Y. Jeong, S. Alam, D. Lin, and D. J. Richardson, Opt. Express **17**, 20927 (2009).
14. B. Ndagano, R. Brüning, M. McLaren, M. Duparré, and A. Forbes, Opt. Express **23**, 17330 (2015).